PNAS RESEARCH ARTICLE | CHEMISTRY OPEN ACCESS

Structured electrolytes facilitate Grotthuss-type transport for enhanced proton-coupled electron transfer reactions

Miguel Muñoz[a], Michael S. Chen[b,c], Giselle de Araujo Lima e Souza[d], Thomas Simunovic[e], Vaishali Khokhar[a], Peisen Qian[f], Jesse Wainright[a], Robert Savinell[a], Andrew Parnell[g], Steven Parnell[h], Rachel C. Kilbride[i,j], Thomas A. Zawodzinski[e], Mark Dadmun[k], Steven G. Greenbaum[d], Joaquín Rodríguez-López[f], Mark Tuckerman[b,c,l,m], and Burcu Gurkan[a,n,1]

Affiliations are included on p. 10.

Edited by Sharon Hammes-Schiffer, Yale University, Princeton, NJ; received October 30, 2025; accepted November 26, 2025

Concentrated hydrogen-bonded electrolytes (CoHBEs) are structured, electrochemically stable, less-volatile alternatives to aqueous and dilute nonaqueous electrolytes, however, with high viscosities that limit molecular diffusion. This work provides an understanding of the proton conduction mechanism in CoHBEs based on mixtures of acids and azoles and establishes a link between the structurally dictated transport properties and the proton-coupled electron transfer (PCET) reaction rates that can be leveraged for enhancing electrochemical reactions. Diffusion and relaxation NMR studies suggest a breaking of the viscosity–conductivity tradeoff, where at high azole concentrations (>45 mol%), Grotthuss transport is more likely with lowered proton transfer energy barriers between the azole and the acid according to the machine learning (ML) accelerated ab initio path integral MD (AI-PIMD) simulations. Proton conduction pathways are found to be switchable between the hydrogen bonding networks of the acid and the azole, with imidazole chain forming structures better facilitating Grotthuss hopping. Supported by small-angle neutron scattering studies, the chains are found to have six member molecules on average with maximum of 3 to 4 imidazole/imidazoliums at 50 to 60 mol%. Despite their high viscosities, the measured PCET rates for quinones and phenazines measured in the protic CoHBEs present relatively high electron transfer rate constants ($k_0 \sim 10^{-4}$ cm/s), validated by rotating disc electrode and scanning electrochemical microscopy measurements. The results demonstrate that strategic tuning of hydrogen-bond donor–acceptor interactions enables the decoupling of proton transport and viscosity, thereby impacting PCET reactions.

eutectic solvents | protic electrolytes | electrokinetics | proton conduction

Concentrated hydrogen-bonded electrolytes (CoHBEs), which broadly encompass ionic liquids and deep eutectic solvents (1), have emerged as promising systems for electrochemical applications where nonflammable and nonvolatile electrolytes are desired (2). Unlike conventional electrolytes, CoHBEs present heterogenous structures and tunable solvation through the pairing of hydrogen bond acceptors and donors (3, 4). CoHBEs offer distinct advantages over aqueous and organic electrolytes. While aqueous systems enable efficient ion conduction, their narrow electrochemical stability window (ESW) limits their applications in various devices such as rechargeable batteries (5). On the other hand, organic electrolytes, despite their broader ESW, are hindered by volatility and safety concerns (6). In contrast, CoHBEs provide a less-volatile, chemically stable alternative with extended ESWs due to their high concentration of salt and/or hydrogen bonds and tunable solubility of active components for advanced energy storage and conversion technologies (2). Despite these advantages, CoHBEs commonly exhibit high viscosities which impedes diffusion of charge carriers and redox species to the electrode surface, often limited by the vehicular ion transport mechanism (7).

Cosby et al. (8) demonstrated the hydrogen-bond network modulation in a protic CoHBE composed of levulinic acid (LA) and 2-ethyl-4-methylimidazole (2E4MIm). They observed that introducing LA to 2E4MIm disrupted slow Debye-like relaxation that led to a 10-fold increase in ionic conductivity. Subsequent ab initio molecular dynamics (AIMD) simulations confirmed the existence of dynamic hydrogen-bonded chains, wherein chain membership changes on a 30 to 40 ps time scale (9). In a separate study, it was confirmed that the antiparallel rigid chains of imidazoles were disrupted by the introduction of specific amounts of LA or butyramide as the underlying mechanism for the enhanced ionic conductivity in these CoHBEs (10). To overcome viscosity-limited transport in CoHBEs, alternative transport mechanisms are needed. Unlike vehicular transport, where species move with their solvation shell and thus exhibit strong viscosity dependence, Grotthuss transport involves rapid hopping through a dynamic reorganization of solvating species (11), such as the

Significance

This work presents a fundamental understanding of the proton conduction mechanism in protic concentrated hydrogen-bonded electrolytes (CoHBEs) (protic ionic liquids in excess of acid or base) that are relevant to energy storage and conversion and electrocatalysis. We elucidate how the dynamic hydrogen-bonded chains that form in mixtures of acids and amphoteric azoles accelerate proton conduction. Consequently, the measured proton-coupled electron transfer (PCET) reactions involving redox-active molecules in these structured electrolytes demonstrate comparable rates to those in conventional electrolytes, despite the low diffusivity of redox species. Our findings provide a molecular-level framework for CoHBEs that leverage molecular substitution, donor/acceptor composition, and the ability of the liquid to form extended hydrogen-bonded chains having symmetrical low proton transfer barriers between its molecular units.

The authors declare no competing interest.

This article is a PNAS Direct Submission.

[1]To whom correspondence may be addressed. Email: beg23@case.edu.

This article contains supporting information online at https://www.pnas.org/lookup/suppl/doi:10.1073/pnas.2530367122/-/DCSupplemental.

Published January 2, 2026.

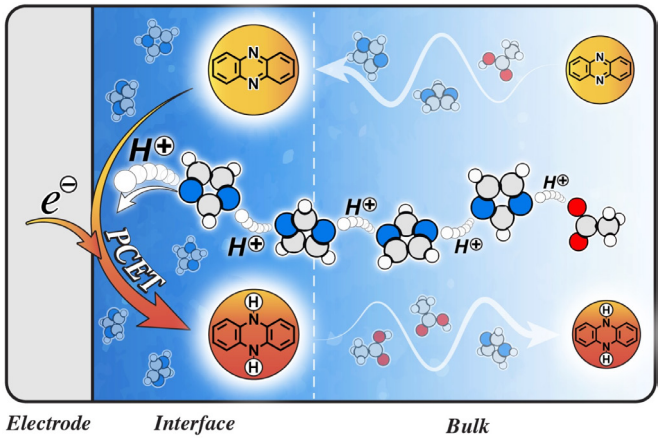

Scheme 1. Illustration of the vehicular transport of the redox-active species from the bulk to the interface and the structural diffusion (Grotthuss type) of proton, facilitated via hopping along the chain structure. At the electrode surface, PCET reaction takes place as illustrated.

structural diffusion of protons along a hydrogen-bond network as illustrated in Scheme 1. This mechanism enables fast ion transport even in highly viscous media and in protic mixtures with relatively low ionic content (12–15). Achieving structural diffusion of protons requires the use of amphoteric species capable of both donating and accepting protons and sustaining flexible hydrogen-bond networks (16). By carefully selecting hydrogen bond donors (HBDs) and hydrogen bond acceptors (HBAs), hydrogen-bond strength and connectivity can be tuned, enabling efficient proton transfer with minimal structural reorganization energies and ultimately optimizing conductivity (17). Proton conduction mechanism is particularly relevant for proton-coupled electron transfer (PCET) reactions, where proton transport efficiency directly impacts charge transfer kinetics (18, 19). Since PCET governs key electrochemical processes in fuel cells, electrocatalysis, and energy storage, understanding hydrogen-bonding networks in protic CoHBEs and their influence on interfacial reactions is important.

In this study, a systematic set of protic CoHBEs derived from the benchmark system of 2E4MIm:LA was examined to understand how variations in HBDs and HBAs influence transport properties and electrokinetics of PCET reactions. Employing ^{1}H-NMR, FTIR, and pulsed field gradient (PFG)-NMR, the structural and dynamic factors influencing proton conduction were studied. Additionally, NMR relaxation experiments were performed to distinguish between fast-exchanging proton species and those involved in strong hydrogen-bonding networks. We performed high-level ab initio path integral MD simulations (AI-PIMD), accelerated with machine learning (ML) potentials, to provide additional microscopic detail into the composition-dependent trends for the identified electrolytes. The structural features were further examined by small-angle neutron scattering (SANS). Redox-active species, specifically the quinone and phenazine derivatives, capable of PCET were incorporated to examine charge transfer kinetics. Rotating disk electrode (RDE) and scanning electrochemical microscopy (SECM) experiments revealed relatively fast electrokinetics despite the high viscosity of CoHBEs, thus underscoring the potential utility of these structured electrolytes for various electrochemical processes.

Results and Discussion

Proton Conduction via the H-Bonding Network. Structures of protic CoHBEs based on 1:1 equimolar HBA:HBD mixtures are shown in Fig. 1*A*, along with the measured viscosity (η) and conductivity (σ) in Fig. 1*B* (data in *SI Appendix*, Table S1). The acetic acid (AA)-based mixtures showed the highest σ and lowest η, with 1MIm:AA as the most extreme case, owing to reduced steric hindrance due to the shorter alkyl chain in AA compared to LA. In the case of 1MIm:AA, N1 methylation may additionally modulate intermolecular interactions by reducing molecular packing; previous studies have shown 1MIm forms short, highly polarized hydrogen bonds with AA which reduce the proton transfer barrier within the acid network (20). The ^{1}H-NMR spectra (*SI Appendix*, Fig. S1 for AA-mixtures and *SI Appendix*, Fig. S2 for LA-mixtures) suggests fast proton exchange between the acid and imidazole components as evidenced by merging of N–H (of the imidazole) and O–H (of the acid) signals into a single peak in mixtures. The AA-based mixtures exhibited the most pronounced downfield shifts, with 1MIm:AA and 1HIm:AA showing the highest chemical shifts (15.26 and 15.07 ppm, respectively), consistent with short and strong H-bonds typically above 14 ppm due to proton delocalization (20). ATR-FTIR spectral features further support hydrogen-bond interactions and H-bond complex formation (*SI Appendix*, Fig. S3). It is worth noting that the relatively low conductivity of the triazole mixtures, despite their low viscosities, is similar to results of prior AIMD simulations where the additional central nitrogen in triazole, not present in imidazole, was found to block the diffusion of the excess proton introduced in simulations by trapping it on triazolium, thereby significantly reducing proton diffusivity (21).

From the overall view of Fig. 1*B* data, contrary to the assumption that a high pKa difference (ΔpKa > 8) between HBD and HBA dictates ideal ionic transport in liquids (22), we see that systems with lower ΔpKa (1HIm:AA; ΔpKa = 2.19 and 1MIm:AA; ΔpKa = 2.64), exhibited higher σ, whereas systems with larger ΔpKa values (>3.5), including 2E4MIm, 123Trz, and 124Trz, did not exhibit as high σ. This suggests that the transport mechanism in these systems deviates from the classical Brønsted-Lowry acid–base expectations. Instead, the effective acid–base behavior evolves with the hydrogen-bonding environment, where local structural organization can shift relative proton affinities. These observations imply that ionic transport in CoHBEs arises from a complex interplay of hydrogen bonding, molecular structure, and proton dynamics rather than from ΔpKa alone. Earlier studies with these types of mixtures, at compositions with low ionic content, also reported high conductivities (12–15).

The composition-dependent σ, η, and density (ρ) are shown for 1HIm:AA in Fig. 1*C* and for 1MIm:AA in Fig. 1*D*. The 1HIm:AA mixture is a solid at 30 to 40 mol% 1HIm and above 70 mol% (also confirmed by DS; *SI Appendix*, Fig. S4). In general, the thermal stability increases with increasing 1HIm mol% (assessed by TGA; *SI Appendix*, Fig. S5), due to the strengthened H-bonding and ionic interactions. Increasing imidazole content raises all three measured macroscopic properties initially: up to 15 mol% for 1HIm and 30 mol% for 1MIm. This increase results from the progressive disruption of AA–AA hydrogen-bonded dimers with the introduction of the imidazole, as evidenced in our ML-driven AI-PIMD simulations (Fig. 2*A*). We find evidence to the existence of ionic species in Raman spectra (*SI Appendix*, Fig. S6 *A* and *B* for 1HIm:AA and *SI Appendix*, Fig. S6 *C* and *D* for 1MIm:AA), similar to a prior report (23). Particularly, distinct vibrations corresponding to the acetate (926 cm^{-1}) and imidazolium (1,212 to 1,233 cm^{-1} for 1HIm; 1,554 to 1,587 cm^{-1} for 1MIm) species are seen with increasing imidazole/imidazolium (Im) content (See *SI Appendix*, Table S2 for all vibrational assignments). Due to the formation of ionic species, the conductivity initially increases with the amount of Im. More quantitative population analyses from simulations (*SI Appendix*, Fig. S7) and the

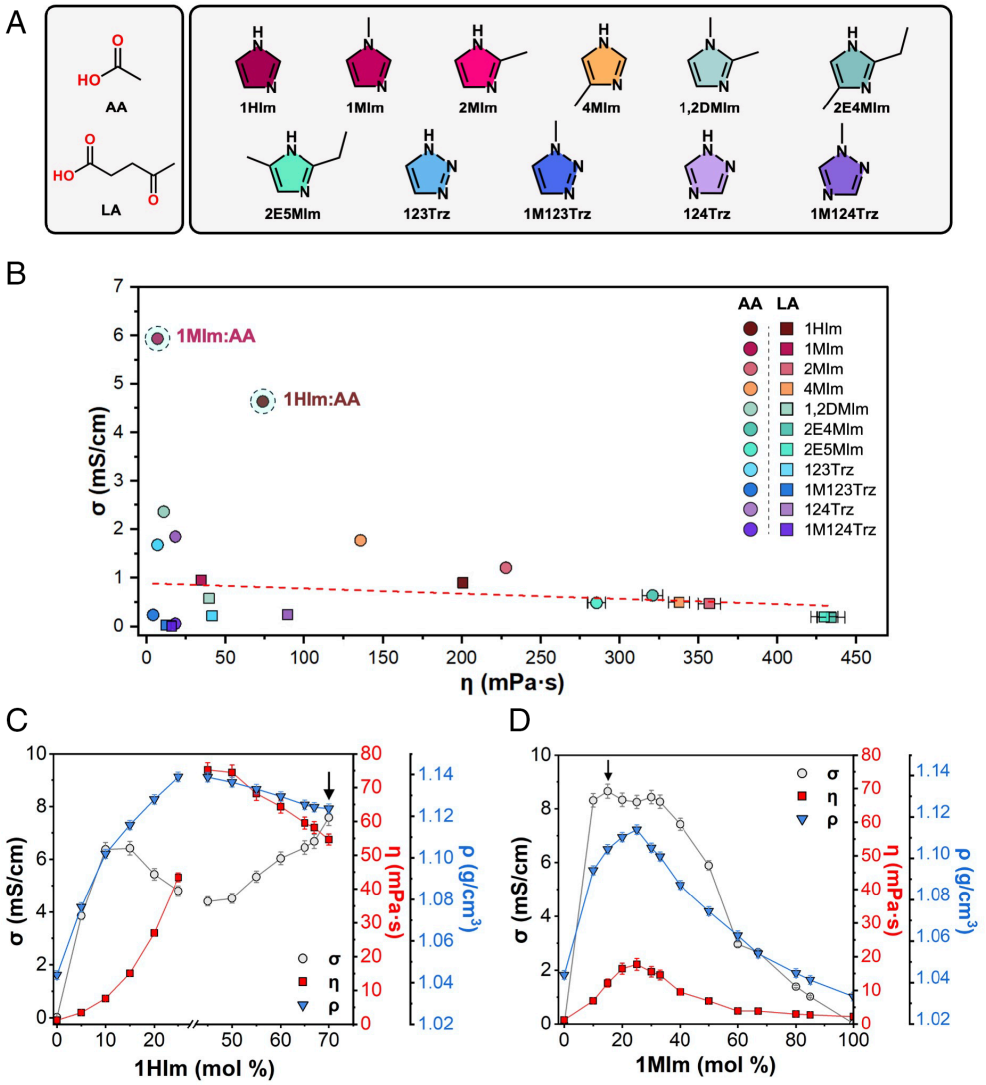

Fig. 1. Molecular structures and transport properties of protic CoHBEs. HBDs and HBAs investigated (*A*) and conductivity (σ) vs. viscosity (η) measured at equimolar HBA:HBD ratios at 298 K (*B*). The dashed line is a linear fit that excludes the two outliers (dashed circled with blue highlight). Circles represent AA-based systems and squares represent LA-based systems. The composition-dependent σ, η, and density (ρ) measured for 1HIm:AA (*C*) and 1Mim:AA (*D*) at 298 K. Arrows mark the compositions selected for electrochemical characterization with redox-active molecules.

atomistically decomposed vibrational density of states (*SI Appendix*, Fig. S8) indicate nearly all of the imidazole molecules at 15 mol% are protonated and the maximum molar population of imidazolium is observed at 50 mol%. The availability of free ions that can contribute to conductivity increases as the persistent AA–AA dimers are weakened with the introduction of imidazole as probed by ionicity (*SI Appendix*, Fig. S9). Beyond 50 mol%, the imidazolium population decreases in conjunction with the increase in the number of hydrogen bonds between imidazole pairs (Fig. 2*A*). Even though the number of ionic pairs goes down beyond 50 mol% (*SI Appendix*, Fig. S7), the effective ionicity conducive to charge transport still increases which lends evidence of Grotthuss transport. We can confirm this by comparing the activation energies of the molar conductivity and fluidity (*SI Appendix*, Fig. S10 for 1HIm:AA) where deviations from a linear relation between the two are observed at 50 to 70 mol% of 1HIm; once again suggesting decoupling between ion motion and viscous flow.

To further explore the proton conduction in 1HIm:AA, PFG-NMR measurements were performed. Fig. 2*B* shows the composition-dependent average diffusivities. At low 1HIm concentrations (5 to 25 mol%), the sharp drop in the average diffusion coefficient indicates the formation of a highly constrained environment. Since the signal of the exchangeable protons originate from both 1HIm and AA, the observed diffusion coefficient (D_{NH-OH}) is expected to correspond to a molar-weighted average of the parent species diffusivities ($D_{NH\text{-}OH(est)}$). However, as the 1HIm content increases beyond 45 mol% 1HIm, experimentally measured D_{NH-OH} surpasses the estimated $D_{NH\text{-}OH(est)}$ (by ≥ 10%). This suggests a transition of proton transport from primarily mediated via AA-based hydrogen-bond network to a more efficient 1Him-based network. Consistent with these observations, the measured hydrogen-bond donor acidity decreases while the hydrogen-bond acceptor basicity increases with higher Im content (*SI Appendix*, Fig. S11), reflecting reduced donor strength and enhanced acceptor capacity in reorganized hydrogen-bond networks. This compositional dependence determined from the solvatochromic studies indicates that effective acidity and basicity are not static properties but shift with local solvation structure, directly supporting the deviations from classical Brønsted–Lowry expectations noted earlier.

To assess molecular motions, ^{13}C NMR relaxation times (T_1) were determined as a function of composition for a series of 1HIm:AA samples. The characteristic timescale of ^{13}C motions

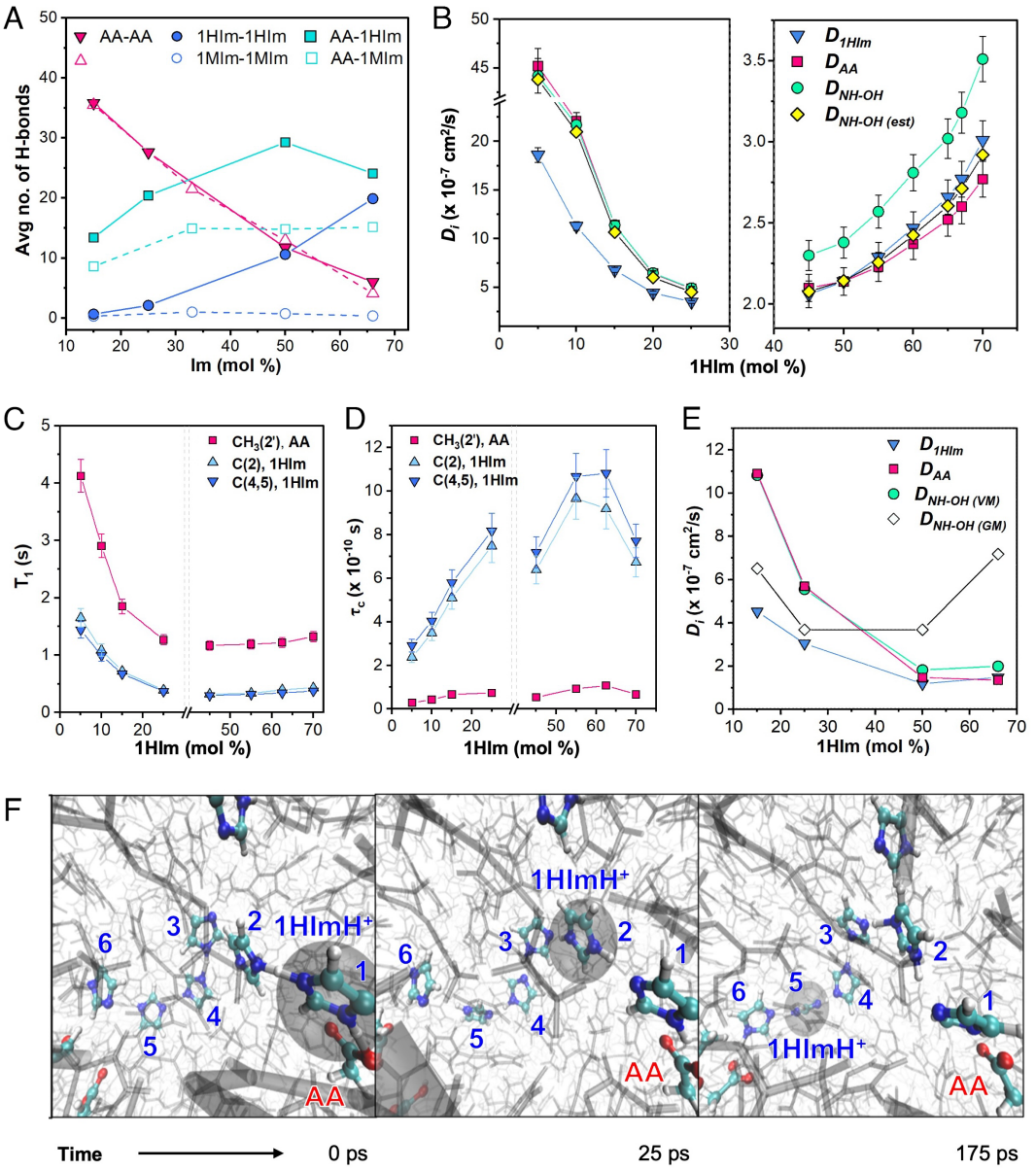

Fig. 2. H-bonds, diffusivities, and relaxation dynamics. Calculated average number of H-bonds from ML accelerated PIMD simulations (*A*): filled symbols are for 1HIm:AA and hollow symbols are for 1MIm:AA. Measured average diffusion coefficients for 1HIm:AA (*B*) at 5 to 25 mol% (*Left*) and 45 to 70 mol% (*Right*). $D_{NH\text{-}OH(est)}$ represents the molar-weighted average of the parent species 1HIm and AA. ^{13}C NMR relaxation times (T_1) for selected carbons as a function of 1HIm composition, probing pico- to nanosecond molecular motions (*C*). Correlation times (τ_C) extracted from T_1 data, highlighting distinct segmental dynamics of methyl groups (AA) relative to 1HIm carbons (*D*). The compositional range where 1HIm:AA mixture solidified at 298 K. The diffusion coefficients obtained from RPMD simulations (*E*) breaks down the diffusivity of the proton defect due to vehicular mechanism (VM) and additionally the Grotthuss mechanism (GM); the total corresponds to the diffusivity of the exchangeable proton as obtained from PFG-NMR for 1HIm:AA. Representative snapshots from RPMD simulations for the mixture with 66 mol% 1HIm (*F*) demonstrate the diffusion of the proton defect (circled in gray) via GM along a hydrogen-bonded chain of 6 imidazole molecules as labeled.

related to local segmental and molecular dynamics, known as the correlation time (τ_C), lies in the pico to nanosecond range and can be estimated by analyzing the relaxation rate ($R_1 = 1/T_1$) in relation to the strength of the ^{1}H–^{13}C interaction. The fraction of the observed R_1 that is associated with that interaction was assessed by determining the nuclear Overhauser effect enhancement (NOEE) of the ^{13}C signal by ^{1}H polarization (*SI Appendix*, Fig. S12). T_1 and τ_C are shown as functions of composition in Fig. 2 *C* and *D*, respectively. The relaxation times of the CH_3 group in AA are systematically longer than those of the ring carbons in 1HImin across the entire composition range (*SI Appendix*, Table S3). The longer T_1 values of the CH_3 group in AA compared to the 1HIm ring carbons are expected, since methyl groups can rotate more freely (24). In contrast, the similar T_1 values for all ring carbons suggest that the imidazole ring undergoes collective reorientation rather than localized segmental motion, as also supported by the comparable correlation times for C(2) and C(4,5), which fall within the same range considering experimental uncertainty. While T_1 levels off beyond 45 mol% Im (Fig. 2*C*), indicative of a stabilized hydrogen bonding network, diffusivity increases in the same region (Fig. 2*B*). This decoupling between translational dynamics and local reorientational motion indicates a change in the dominant charge transport mechanism, suggesting a transition to more efficient proton transport despite minimal changes in localized molecular mobility. Ring-polymer molecular dynamics (RPMD) simulations provide direct evidence of Grotthuss transport of proton defects along hydrogen-bonded chains, allowing us to track and quantify their diffusion

accelerated by the Grotthuss mechanism. Fig. 2*E* shows the breakdown of the proton diffusion into contributions from vehicular mechanism ($D_{NH\text{-}OH\ (VM)}$) and additionally from the Grotthuss mechanism ($D_{NH\text{-}OH\ (GM)}$) which is particularly elevated at 50 mol% 1HIm and beyond. The snapshots from the simulations at times 0, 25, and 175 ps in Fig. 2*F* illustrate the diffusion of the proton defect.

In the condensed-phase AIMD simulations, we found that the proton transfer barriers between the imidazole and the acid are sensitive to the average local environment at different compositions (Fig. 3 *A* and *B*). The difference between 1HIm:AA and 1MIm:AA lies in the direction of the proton shuttling where the proton tends to localize on Im with 1HIm (Fig. 3 *A*, *Left*) at the highest Im content and on the acid with 1MIm (Fig. 3 *B*, *Left*). For proton transfers between 1HIm and AA, the energy minima occur when the proton is covalently bonded to imidazole ($r_{NH^*} < r_{OH^*}$), with virtually no barrier. As the 1HIm content increases, the asymmetry in the barrier decreases, suggesting enhanced proton delocalization along the hydrogen-bonded networks. Despite minor 1MIm–1MIm H-bonding (Fig. 2*A*), no proton transfer is observed. On the other hand, the number of hydrogen bonds between imidazoles (blue symbols) increases with increasing 1HIm content as seen in Fig. 2*A*. This is accompanied by a similar increase of H-bonds between AA-1HIm (green symbols) up to 50 mol% but with a subsequent decrease at 66 mol%. This is consistent with the formation of more extended Im chains with increasing mol% 1HIm observed in the PIMD simulations as seen in the plotted probability densities calculated for the hydrogen-bonded chains in Fig. 3*C*. For 1HIm:AA mixtures, there are roughly six members in a chain with 3 to 4 Im molecules on average at 50 to 66% Im. The SANS data obtained with mixtures of deuterated 1HIm and protonated AA mixtures at 15, 30, 50, and 70% Im in Fig. 3*D* reveal a persistent scattering feature at q ≈ 0.5 to 0.7 $Å^{-1}$, corresponding to a length scale of 9 to 13 Å commensurate of 3 to 4 units of Im. While the simulated chains are not necessarily linear and/or extended, the general agreement between the SANS and PIMD results support the existence of hydrogen-bonded chains.

Further structural analysis by NMR and FTIR corroborates the composition-dependent structural changes discussed. The downfield shifts are observed in ^{1}H NMR spectra for NH(1)–OH(1') signal in Fig. 4*A* for 1HIm:AA (*SI Appendix*, Fig. S13, full spectra) and N-OH(1') signal for 1MIm:AA in Fig. 4*B* (*SI Appendix*, Fig. S14, full spectra). These shifts (0.4 to 2.8 ppm) are significant

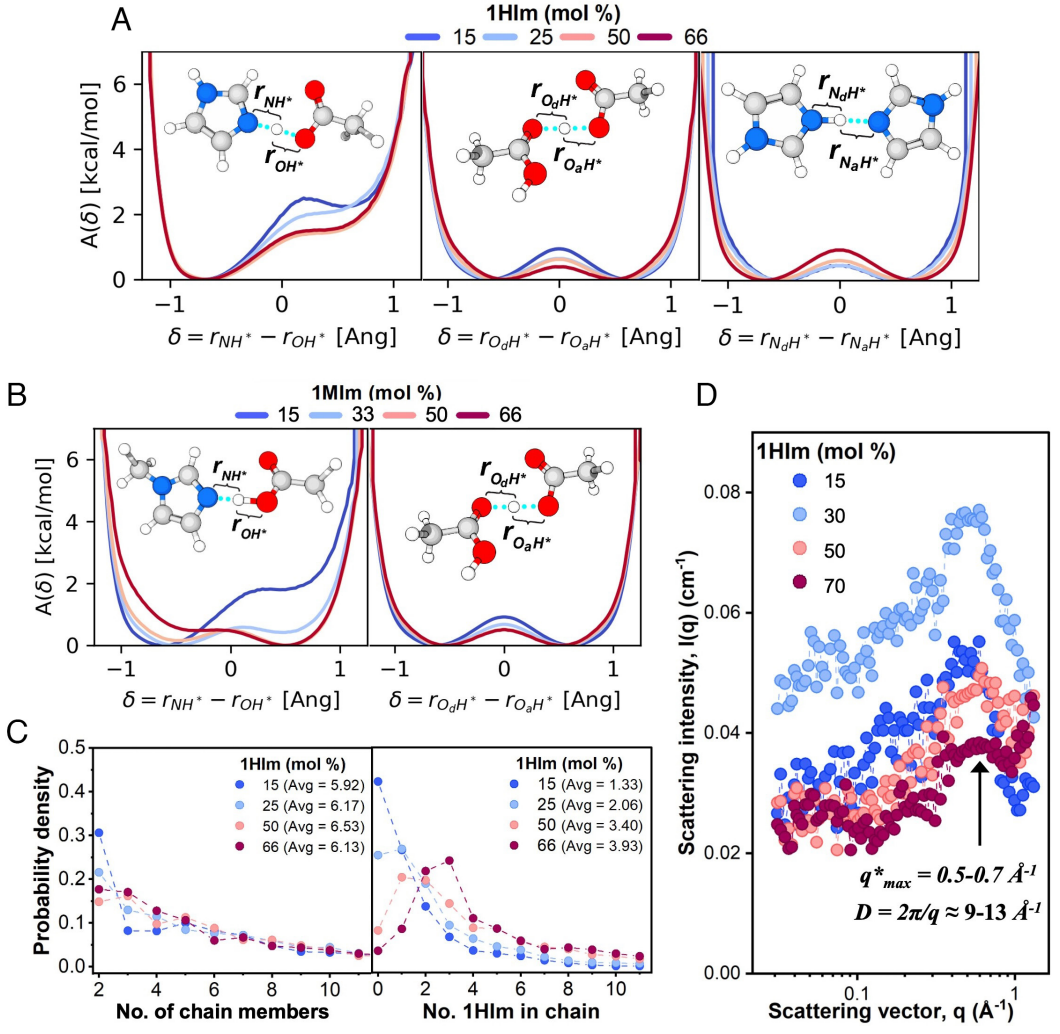

Fig. 3. Proton transfer energy barriers and liquid structure. Calculated proton transfer energy barriers, A(δ), between Im–AA, AA–AA, and Im–Im, from PIMD simulations with nuclear quantum effects for 1HIm:AA (*A*) and 1MIm:AA (*B*). Probability distributions of hydrogen bond chain length (*C*), in terms of the number of molecules that constitute the chain (averages are noted in parentheses), and the number of imidazole/imidazolium molecules that make up a given chain for 1HIm:AA mixtures as obtained from PIMD simulations. SANS data showing structural features as a function of deuterated 1HIm in protonated AA (*D*).

for high-resolution ^{1}H NMR and are consistent with the enhancement of proton delocalization with more structured hydrogen-bonding network and enhanced Im–AA interactions as reported in analogous Im–acid systems (16). In contrast, the ring (4, 5) and alkyl (6) protons shift progressively upfield with increasing Im content, reflecting reduced local polarization and composition-dependent averaging toward neutral Im, as in prior reports on heteroaromatics (25). Further, the methyl resonance of AA (2') also shifts upfield with increasing Im fraction, which may be linked to changes in acid speciation between dimers and acid–base complexes. Beyond 50 mol% Im, a very slight upfield shift observed for NH···OH again suggests H-bond reorganization due to excess Im disrupting the donor-acceptor balance. While the spectral shifts in Fig. 4 *A* and *B* mirror the observed η trends in Fig. 1 *C* and *D*, respectively, where the system transitions from a rigid hydrogen-bonded phase to a more mobile regime, trends in σ deviate between these two systems (1MIm *vs.* 1HIm). For 1HIm:AA, the amphoteric nature of 1HIm combined with enhanced fluidity in high-σ regime, likely presents a more flexible hydrogen-bond network that facilitates enhanced proton diffusion. However, for 1MIm:AA, N1-methylated azole cannot sustain extended proton-conductive structures; therefore, σ decreases at higher 1MIm content. It is possible that both systems have some extent of Grotthuss transport; however, the structural features that accelerate proton conduction (imidazole *vs.* acid domains) vary between the two systems as a function of composition.

FTIR spectra (*SI Appendix*, Fig. S15 experimental; *SI Appendix*, Fig. S8 simulated) present two main vibrations that are informative of the local structure: ν(N–H) and ν(C = O). The N–H stretching band of Im, ν(N–H), observed in the 3,156 to 3,116 cm^{-1} range is significantly red-shifted (Fig. 4*C*) from the typical free N–H vibrations (3,300 to 3,500 cm^{-1}) indicating the formation of directional N–H···O bond, similar to observations in protic ionic liquids (26–28). In parallel, ν(C = O) shows an initial blue-shift (1,704 → 1,709 cm^{-1}) with an increase in transmittance up to 25 mol% of 1HIm (Fig. 4*D*). Upon reentering the liquid phase (≥45 mol%), ν(C = O) shows a red-shift (1,706 → 1,702 cm^{-1}), suggesting renewed polarization through NH···O = C hydrogen bonding. Another informative feature to note is the emergence of broad IR bands attributed to combination modes and overtones (2,730 to 2,220 cm^{-1} and 2,180 to 1,800 cm^{-1} in *SI Appendix*, Fig. S15, *Left*) upon mixing AA with the imidazoles; these are associated with strongly hydrogen-bonded complexes (20, 29), and often linked to proton-shuttling vibrations with large transition dipole moments (30). In 1HIm:AA, their absorbance increases significantly between 45 to 70 mol% 1HIm (*SI Appendix*, Fig. S15) coinciding with the rise in σ and D_{NH-OH}, reflecting stronger bond polarization and more dynamic proton exchange processes. The structural motifs of the hydrogen-bonding complexes that give rise to these vibrational features play an important role in modulating the proton transfer free energy barriers (31), contributing in part to the composition-dependent trends obtained for the barriers from the ML-driven AI-PIMD simulations.

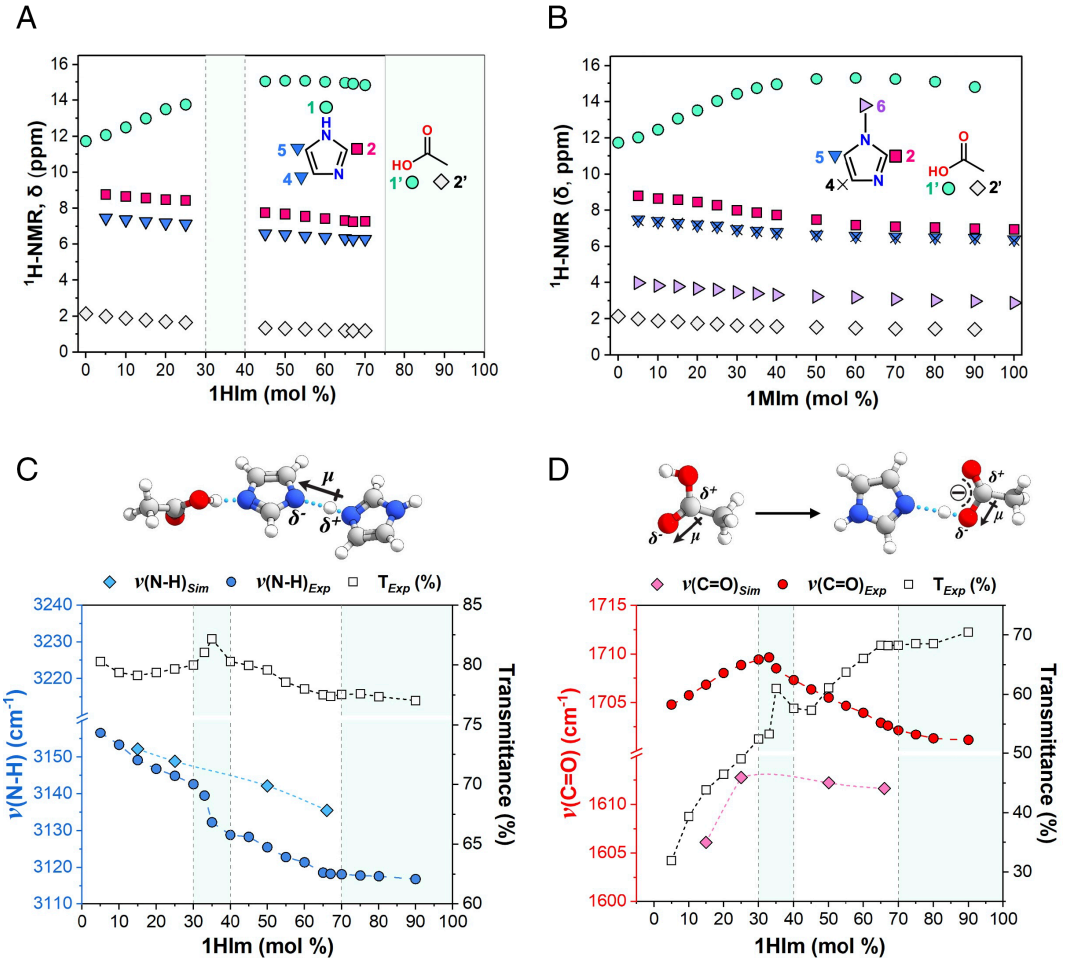

Fig. 4. Composition dependence of the proton shifts and vibrational frequencies. ^{1}H-NMR chemical shifts of 1HIm:AA (*A*) and 1MIm:AA (*B*). FTIR spectral shifts of ν(N–H) (*C*) and ν(C = O) (*D*) stretching modes are shown as a function of composition, along with corresponding simulated peak positions extracted from the computed vibrational density of states for 1HIm:AA. The green-shaded region indicates the composition range where the sample is solidified at 298 K.

Influence of Proton Conduction on PCET Kinetics. Overcoming proton transport challenges in viscous electrolytes by Grotthuss-type conduction is hypothesized to enhance electron transfer rates in PCET reactions. To probe this, kinetic studies of PCET reactions involving various quinone and phenazine derivatives were performed (Fig. 5). Confirming that the ESW of the CoHBEs are sufficiently wide (*SI Appendix*, Fig. S16) to perform the redox reactions of interest, PCET reactions in 1HIm:AA (70:30) and 1MIm:AA (15:85) were examined at the composition corresponding to the maximum macroscopic conductivities. Although the detailed mechanism is not examined here, the presence of a single redox process in the cyclic voltammograms (CVs) is interpreted as corresponding to an overall 2-electron and 2-proton transfer reaction, typical of PCET in protic media (32, 33). As an example, the reduction of phenazine in an acetonitrile-based electrolyte shows two distinct potentials for the two electron transfer reactions, each corresponding to a single-electron transfer (*SI Appendix*, Fig. S17); these reactions appear at the same potential when the protic CoHBE is introduced with a twofold increase in current.

Based on the CV curves corresponding to the PCET reactions of interest, overall smaller potential difference between the reduction and oxidation reactions or the peak separation (ΔEp) is observed in 1HIm:AA compared to 1MIm:AA, suggesting more favorable (faster) electron transfer kinetics. However, slightly asymmetric current responses indicate that while strong hydrogen bonding stabilizes the reduced (e.g., hydroquinone) species, it may also hinder the oxidation step, potentially due to limited proton reorganization dynamics associated with solvent reorganization energy and dynamics (34, 35). To further investigate the electrochemical behaviors, anthraquinone (AQ), phenazine (Phen), and 2,3-diaminophenaizne (DNH_2Phen) were selected as the systems exhibiting the most reversible electron transfer reactions as confirmed by CVs performed at varied scan rates (*SI Appendix*, Figs. S18–S23, panels *A* and *B*; parameters listed in *SI Appendix*, Tables S4 and S5). While AQ demonstrated oxidation irreversibility, particularly at higher scan rates, phenazines presented nearly ideal peak symmetry. Phenazines with their redox-active nitrogen centers fully embedded within an aromatic backbone minimize solvent interactions, thus enabling more efficient (or less) structural reorganization during the redox cycle. Particularly, the reaction rate constant, k_0, that is determined by the Koutecký–Levich analysis using the RDE data (*SI Appendix*, Figs. S18–S23, panels *C*–*F*), reflects the overall $2H^+/2e^-$ transfer rates that are independent of the mass transport of the redox species. Accordingly, phenazines present larger k_0 as summarized in *SI Appendix*, Table S6. The charge transfer coefficients evaluated in this way are related to the mechanism and rate determining steps with anodic and cathodic transfer coefficients summing to the overall number of electrons involved (n = 2 in these cases). The redox molecule Phen was also investigated by SECM. A schematic of the experimental SECM setup is shown in *SI Appendix*, Fig. S24*A* where a 25 μm diameter Au ultramicroelectrode (UME) is positioned above a glassy carbon substrate to enable a localized feedback loop. In the SECM-based kinetic measurement method, the substrate reaction rate constant is correlated with normalized UME tip current, as illustrated in *SI Appendix*, Fig. S24*B*. The extracted k_0 for the oxidation reaction ($PhenH_2 \rightarrow$ Phen + $2H^+$ + $2e^-$), by fitting the kinetic current apparent rate constant as a function of overpotential (η) using Butler–Volmer analysis, suggests marginally faster interfacial kinetics in the 1HIm-based system (Fig. 6*A*) compared to the 1MIm-based system (Fig. 6*B*) at 15 mol% Im. The kinetic rate-limiting values, indicated by dashed lines are derived from the mathematical relations as represented in *SI Appendix*, Fig. S24*C*.

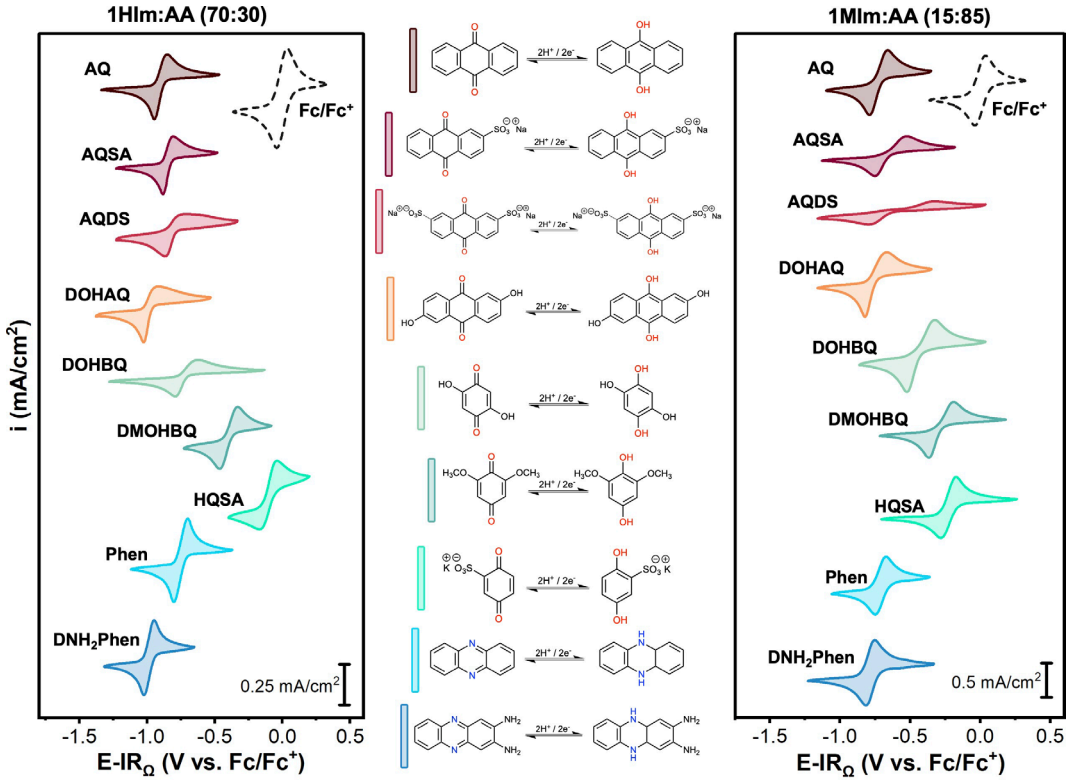

Fig. 5. Cyclic voltammograms of the redox-active species. The redox reaction of the quinone or phenazine at 5 mM was studied by CV in the 1HIm:AA 70:30 (*Left*) and 1MIm:AA 15:85 (*Right*). CVs were recorded at 50 mV/s with a conventional three electrode configuration with glassy carbon working electrode, Pd/PdH reference electrode, and Pt mesh counter electrode, under N_2 atmosphere at 295 K.

Acknowledging that the limited kinetic overpotential window of viscous electrolytes makes it difficult for kinetic analyses of SECM data by Butler–Volmer type fitting, we focus on the general observable trends. Specifically, when comparing the measurable overall reaction rates by RDE, a clear trend emerges for 1HIm:AA and 1MIm:AA mixtures as HBD:HBA composition was varied (Fig. 6*D*). The dependence of k_0 on composition, and hence the extent and type of the hydrogen bonding network, follows the same trend of bulk transport properties for these systems. For example, k_0 for 1HIm:AA decreases from 15 to 50 mol% and rises sharply at 70 mol%, consistent with the changes in conductivity (gray circles in Fig. 1*C*); and D_{Phen} followed the same compositional dependency as does the viscosity. SECM data exhibit the same trend (see *SI Appendix*, Fig. S24*D* for 50 mol% 1HIm where k_0 is minimal at 3.47×10^{-5} cm/s as compared to those shown in Fig. 6*A*).

Fig. 6 *E* and *F* provides a perspective summary on the redox behavior (ΔEp and i_{pc}/i_{pa}) assessed by CV, k_0 for the reduction reaction (e.g., Phen + $2H^+ + 2e^- \rightarrow PhenH_2$) as measured by RDE, and the solubility and diffusivity of the redox species as determined by UV-Vis and RDE, respectively, in the protic CoHBEs of 1HIm:AA (70:30) and 1MIm:AA (15:85). In 1MIm:AA, all three redox species exhibit relatively high diffusion coefficients (> 10^{-6} cm^2/s)—an order of magnitude higher than those in 1HIm:AA. Despite this difference, the calculated k_0 remain comparable between both media, on the order of 10^{-4} cm/s for all redox

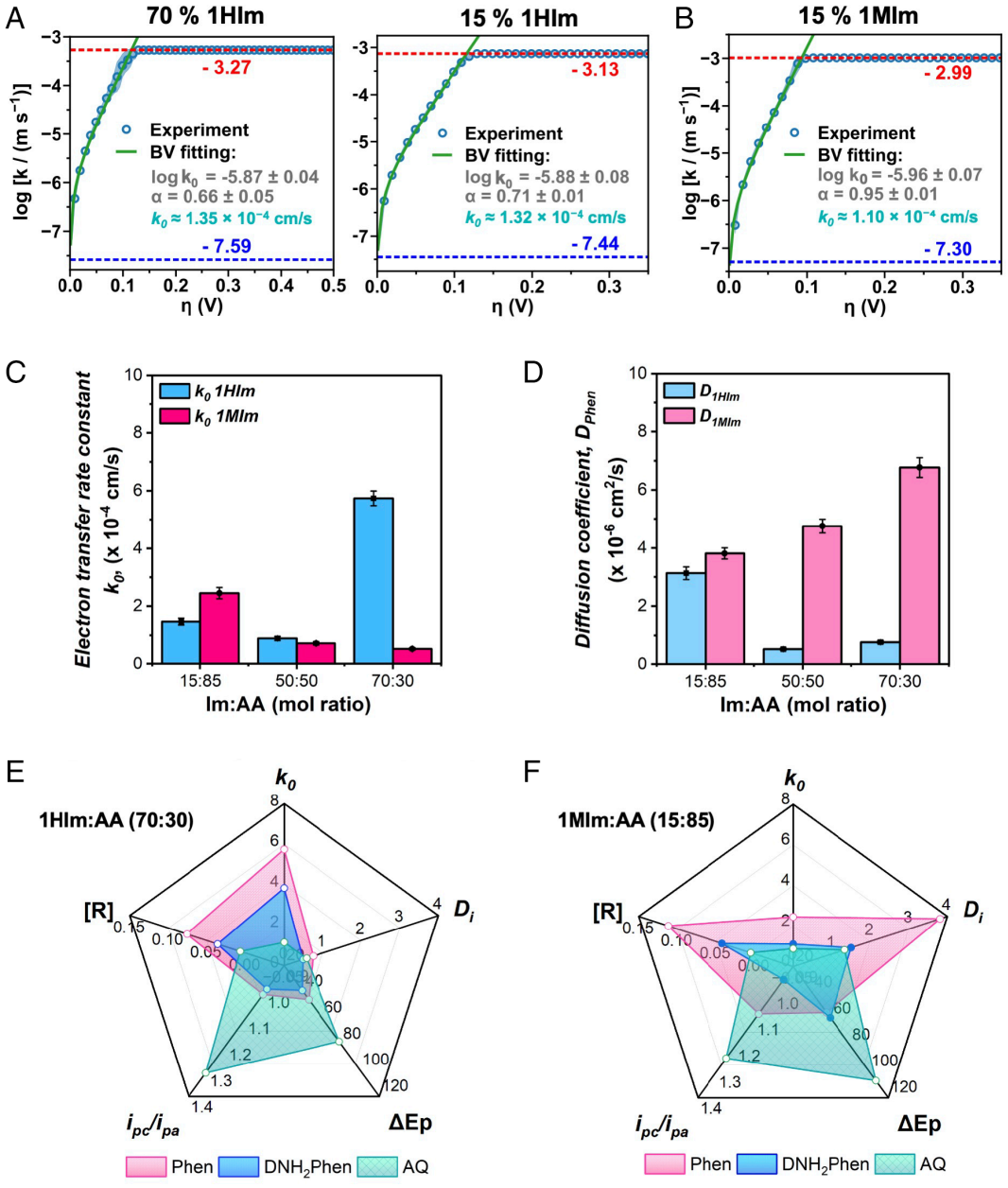

Fig. 6. Kinetics by SECM and RDE and perspective on key electrolyte properties. SECM results for phenazine oxidation kinetics in 1HIm:AA (70:30 and 15:85) (*A*) and 1MIm:AA (15:85) (*B*). The upper (red) and lower (blue) bounds for kinetic measurements are marked by the dashed lines. Reference electrode: Ag/Ag^+; SECM tip (working electrode 1): 25 μm Au UME (ultramicroelectrode); substrate electrode (electrode 2): glassy carbon; Counter electrode: carbon rod. Comparison k_0 (*C*) and diffusion coefficient (D_{Phen}) for phenazine (*D*) in 1HIm:AA (blue) and 1MIm:AA (red) at different compositions as obtained from RDE analysis. Radar plots for a perspective on the composition-dependent differences in redox kinetics, reversibility, and solubility across the two protic CoHBEs: standard rate constant ($k_0 \times 10^{-4}$ cm/s) as determined from the reduction kinetics in RDE measurements, diffusion coefficient ($D_i \times 10^{-6}$ cm^2/s), peak separation (ΔEp, mV), cathodic-to-anodic peak current ratio (i_{pc}/i_{pa}) at 62.5 mV/s, and solubility ([R] in molarity) for phenazine (Phen), 2,3-diaminophenazine (DNH_2Phen), and anthraquinone (AQ) in 1HIm:AA (*E*) and 1MIm:AA (*F*).

couples. These comparable kinetics may reflect different underlying pathways that facilitate charge transport in each system; for example, through extended 1HIm-based hydrogen-bonded networks in 1HIm:AA and through AA association structures in 1MIm:AA. Despite the discrepancies in the absolute k_0 values between the RDE and SECM methods (expected given the different mass transport regimes and local interfacial conditions probed), the general agreement on compositional dependency of electrokinetics for the overall reactions supports the original hypothesis on proton conduction enhancing PCET rates.

The measured solubilities determined by UV-Vis measurements (*SI Appendix*, Table S7) range between 5 and 164 mM at about 22 °C. As seen in Fig. 6*E*, Phen exhibited greater solubility in 1MIm:AA solvent (112 mM) compared to 1HIm:AA (76 mM). The solubility is influenced by several factors, including the polarity of the molecules, π–π interactions, acid–base interactions, and the strength of hydrogen bonding. The limited solubilities suggest strong solvent–solvent and suboptimal solute–solvent interactions. Molecular derivatization of Phen may increase solubility and further tune the redox potential for an increased cell voltage, thus advancing protic CoHBEs for flow batteries based on PCET reactions.

The obtained redox species diffusivities are comparable to the measured self-diffusion coefficients of the electrolyte components in this study as well as the previously determined diffusivities in aqueous electrolytes [e.g., ~10^{-6} cm^2/s for phenazines (33)]. This similarity suggests that ion pairing or strong association effects are not predominant in the CoHBEs under the conditions examined. Similarly, the redox-active protic CoHBEs exhibit moderate to fast electron transfer rates (k_0 ~10^{-4} cm/s) with Phen displaying the fastest kinetics. Again, the measured rate constant is similar to the rate constants reported for phenazines in aqueous electrolytes (i.e., 1.0 M KCl) (33). In contrast to 1MIm:AA, the diffusivities are approximately one order of magnitude lower (~10^{-7} cm^2/s) in 1HIm:AA, consistent with a more structured hydrogen-bond network. Furthermore, k_0 values for 1HIm:AA are higher than those values reported in CoHBEs such as ethaline (often below 10^{-6} to 10^{-7} cm/s) (36). However, the kinetics are one order of magnitude lower than the highest reported PCET rates in aqueous media, such as 1.15 × 10^{-3} cm/s for 2,2′-(phenazine-1,8-diyl)bis (ethane-1-sulfonate) in 1.0 M KOH (37).

The values of the apparent cathodic charge transfer coefficient, alpha (α_c), observed for AQ, DNH_2Phen, and Phe, (*SI Appendix*, Table S6) are similar to prior reports in aprotic CoHBEs (36, 38, 39). The values of α_c near unity for DNH_2Phen, and Phe are in agreement with a symmetrical one-step two-electron reaction. In the case of AQ, the larger value of α_c might be related to a rate limiting first one-electron transfer step followed by a second fast one-electron transfer step. More complex mechanisms involving proton or reactant adsorption might also be involved in all three of these reaction couples (39). Literature supports the notion of Grotthuss conduction of protons enhancing interfacial reactions (40, 41), including an analogous PCET reaction such as that with diaminobenzoic acid at a modified glassy carbon electrode where the concerted proton–electron transfer reaction was accelerated in the presence of hydronium/water donor/acceptor pair (19). Accordingly, the observed apparent charge transfer coefficients were greater than 0.5, similar to the case in this study, as a result of proton transport enabled by Grotthuss hopping which may indicate low transition state barriers. While the detailed analysis of the electrokinetics and the rate parameters require further development of a reaction model with mechanistic steps, this study points to the tunable nature of CoHBEs for enhancing PCET rates through the proton conducting structural networks.

Conclusions

This work establishes a molecular-level framework for advancing CoHBEs that enable efficient proton transport and redox activity. Mixtures of imidazole and acetic acid present lowered proton transfer barriers at compositions that support the formation of imidazole-imidazolium percolating structures. Fast proton conduction along such structures are shown to enhance PCET kinetics. While PCET reactions are essential for photosynthesis and respiration, they are also highly relevant to electrocatalytic and energy storage and conversion processes. Specifically, in the context of flow batteries where redox-active species are solubilized in the supporting electrolyte, CoHBEs present the possibility of extending the cell potential for enhanced energy and power densities while maintaining battery safety.

Materials and Methods

Materials and Sample Preparation. High-purity reagents as provided in *SI Appendix*, Text S1 were used in sample preparation. To ensure minimal water content, imidazole and triazole derivatives were dried in a vacuum oven for a minimum of 48 h at 323 K. Liquid HBAs were dried over 4A molecular sieves (Sigma Aldrich); LA and AA were dried using anhydrous Drierite desiccant (10 to 20 mesh with indicator, VWR). The protic mixtures were prepared by combining the HBAs and HBDs at the specified molar ratios. All sample handling and preparation were conducted in a VTI Super Glove Box (<0.1 ppm H_2O and O_2) purged with Argon (100% Ar, Airgas) to prevent moisture contamination. Samples were characterized by ^{1}H-NMR and FTIR spectroscopy to confirm structural integrity; water content was determined to be below 500 ppm for all samples, using Karl Fischer titration (Metrohm Coulometric; KF 889D) (water contents are listed in *SI Appendix*, Table S8 for 1HIm:AA and *SI Appendix*, Table S9 for 1MIm:AA). Thermal analysis was performed by differential scanning calorimetry (Mettler Toledo DSC) and thermal gravimetric analysis (TGA500, TA Instruments) to confirm the liquidus range and thermal stability as described in *SI Appendix*, Text S1. The reported onset temperatures (T_{onset}) in *SI Appendix*, Table S10 correspond to the temperature at which a 5% mass loss occurred. Physical properties, including density, viscosity, and ionic conductivity measurements were performed as described in our prior report (42). The measured macroscopic properties (density, viscosity, and conductivity) are tabulated in *SI Appendix*, Tables S8 and S9 for 1HIm:AA and 1MIm:AA, respectively.

Spectral Analyses for H-Bonding and Transport. FTIR spectroscopy with attenuated total reflection (ATR) was conducted using a Nicolet iS50 Thermo Scientific spectrometer equipped with a single-reflection diamond ATR. Spectra were recorded over a range of 450 to 4,000 cm^{-1} with a resolution of 1 cm^{-1}. For ^{1}H-NMR and self-diffusion coefficients measurements by PFG-NMR, samples were placed in 5 mm NMR tubes containing a flame-sealed capillary tube of deuterated dimethylsulfoxide (DMSO-d6) and tetramethylsilane, serving as the lock signal and chemical shift reference, respectively. For the measurement of ^{13}C spin-lattice relaxation, samples were prepared in an Argon glovebox and sealed in a J-Young NMR tube with a flame-sealed D_2O capillary. The samples were prepared in this way to prevent water and oxygen uptake. NOEE experiments were run on the 1HIm:AA system. The PFG-NMR and NOEE details are provided in *SI Appendix*, Text S2. The estimation of ionicity (values in *SI Appendix*, Table S11) is detailed in *SI Appendix*, Text S3. Raman spectra were collected at 298 K with an InVia, Renishaw Raman microscope equipped with a 633 nm excitation laser; details in *SI Appendix*, Text S4. As a reference, the Raman spectra of CoHBE parent compounds AA, 1HIm, and 1MIm are provided in *SI Appendix*, Fig. S25.

Solubility of Redox-Active Species. To determine the solubility of the redox molecule using UV-Vis spectrophotometry, a calibration curve (*SI Appendix*, Fig. S26) was developed from standard solutions. The maximum solubility of the respective redox molecule was determined by measuring the absorbance of a saturated sample and interpolating the concentration value from the established calibration curve. Solvatochromic studies were performed by the same UV-Vis setup using nitroaniline and *N, N*-diethyl nitroaniline dyes. Details to measurements by UV-Vis and estimation of Kamlet-Taft parameters are provided

in *SI Appendix*, Text S5. While FTIR, UV-Vis, and solubility measurements were conducted outside the glovebox, the samples once prepared under an inert and dry atmosphere were then carefully transferred from the glovebox in sealed vials to minimize humid air exposure.

Small-Angle Neutron Scattering. SANS measurements were conducted at room temperature using the D33 SANS instrument at the Institute Laue Langevin in Grenoble, France in time-of-flight (ToF) mode (43). Samples of deuterated imidazole and protonated acetic acid were prepared prior to arrival, sealed in airtight vials, and subsequently transferred to 1 mm path length banjo cells. The D33 diffractometer was configured with sample-to-detector distances $D_{s-d1} = 13.4$ m for the rear detector and $D_{s-d2} = 6$ m for the enclosing four-panel front detector bank. A polychromatic neutron beam with a cutoff wavelength of 14 Å was used, yielding a usable ToF wavelength range of 1.5 to 12 Å and momentum transfer (q) range of ~0.003 to 2.19 $Å^{-1}$. The isotropic two-dimensional (2D) scattering data were converted into one-dimensional (1D) scattering intensity as a function of the wavevector, $q = 4\pi \sin(\theta/2)/\lambda$, where λ is the neutron wavelength and θ is the scattering angle. The acquired scattering data were reduced, calibrated, and corrected for empty cell scattering, acetic acid scattering, detector nonlinearity, electronic noise, stray scattering, sample transmission, and incoherent background scattering using GRASP (44). Subsequently, the data were normalized to absolute differential scattering cross-section and reported in cm^{-1}. SANS data are available at https://doi.ill.fr/10.5291/ILL-DATA.9-10-1891.

Electrochemical Measurements. CV experiments were conducted using a BioLogic SP-240 electrochemical workstation at 298 K (±1 K) within a VTI Super Glove Box (<0.1 ppm H_2O and O_2) purged with argon (100% Ar; Airgas). Ohmic resistance corrections (85% iR compensation) were applied based on the solution resistance obtained from an impedance measurement at 100 kHz with a 20-mV amplitude. A three-electrode configuration was used, comprising a glassy carbon working electrode (BASi, 3 mm diameter; 0.0707 cm^2 area), a palladium hydride (PdH) reference electrode, and a platinum mesh counter electrode. The PdH electrode was prepared by electroplating palladium onto a 0.3 mm platinum wire in a solution of 1 M HCl, 0.28 M $PdCl_2$ and 0.93 M NH_4Cl at −0.2 mA for 30 min. Before use, it was charged in the electrolyte (−0.2 mA for 10 min) and housed in a sealed glass compartment with a glass frit to ensure ionic conduction. All scans were conducted at a fixed rate of 50 $mV{\cdot}s^{-1}$, unless otherwise specified. RDE and linear sweep voltammetry experiments were performed using a three-electrode cell configuration comprising a glassy carbon rotating disk electrode (5 mm diameter, 0.196 cm^2 area; Teflon-encased Pine Research GC disk), a PdH reference electrode, and a platinum mesh counter electrode. Following sample preparation, a continuous nitrogen flow over the sample was maintained to prevent air and moisture exposure during kinetic measurements. Details of the electrokinetic analysis by RDE are in *SI Appendix*, Text S6. SECM was employed to confirm the measured electrokinetics, following a similar protocol reported earlier (45). The details of SECM kinetic analyses are in *SI Appendix*, Text S7.

Theoretical Calculations. ML potentials (MLP) trained to density functional theory (DFT) energies and forces were used to accelerate our MD simulations. Details of the MLP and DFT calculations are in *SI Appendix*, Text S8; details to MD simulations are in *SI Appendix*, Text S9. All MD simulations were performed using periodic simulation boxes with 60 total molecules varying the ratio of molecules accordingly and employing the corresponding experimental densities (*SI Appendix*, Table S12). For the 1MIm:AA simulations, this amounted to including 9, 20, 30, and 40 1MIm molecules for 15, 33, 50, and 66 mol% 1MIm. For the 1HIm:AA simulations, this amounts to including 9, 15, 30, and 40 1HIm molecules for 15, 25, 50, and 66 mol% 1HIm. PIMD and ring polymer MD (RPMD) simulations were employed to incorporate nuclear quantum effects (46). The importance of nuclear quantum effects are highlighted in the *SI Appendix*, Fig. S27 where the proton transfer energy barriers obtained from classical MD show strikingly different results than those obtained by PIMD. PIMD simulations details and FTIR spectral analysis are in *SI Appendix*, Text S10. All simulations were run using our MLPs interfaced to a modified version of the i-PI (46) MD package. Benchmarking for the DFT functional on the basis of computed diffusivities by RPMD is demonstrated in *SI Appendix*, Fig. S28. The mean square displacements used to compute diffusivities are shown in *SI Appendix*, Fig. S29; radial distribution functions used to determine cutoff distances for classifying hydrogen bonding is shown in *SI Appendix*, Fig. S30; and the imidazolium lifetime correlation functions used to examine chain dynamics is shown in *SI Appendix*, Fig. S31.

Data, Materials, and Software Availability. Study data are included in the article and/or *SI Appendix*. Additionally, all data and codes are made publicly available and machine searchable at The Open Science Framework (47).

ACKNOWLEDGMENTS. This study was funded by Breakthrough Electrolytes for Energy Storage Systems–an Energy Frontier Research Center of the United States Department of Energy, Office of Science, Basic Energy Sciences under Award # DE-SC0019409. M.S.C. was supported as a fellow of the Simons Center for Computational Physical Chemistry (SCCPC) at New York University (NYU) (SCCPC, Simons Foundation Grant No 839534). This work was supported in part through the NYU IT High Performance Computing resources, services, and staff expertise, and simulations were partially executed on resources purchased by the SCCPC. We gratefully acknowledge use of the research computing resources of the Empire AI Consortium, Inc, with support from the State of New York, the Simons Foundation, and the Secunda Family Foundation, and the award of SANS beamtime under experimental number 9-10-1891 on the D33 diffractometer at the Institut Laue-Langevin, Grenoble, France.

Author affiliations: [a]Department of Chemical and Biomolecular Engineering, Case Western Reserve University, Cleveland, OH 44106; [b]Department of Chemistry, New York University, New York, NY 10012; [c]Simons Center for Computational Physical Chemistry at New York University, New York, NY 10003; [d]Department of Physics and Astronomy, Hunter College, City University of New York, New York, NY 10065; [e]Department of Chemical and Biomolecular Engineering, University of Tennessee, Knoxville, TN 37996; [f]Department of Chemistry, University of Illinois Urbana-Champaign, Urbana, IL 61801; [g]School of Mathematical and Physical Sciences, University of Sheffield, Sheffield S3 7RH, United Kingdom; [h]ISIS Neutron and Muon Source, Science and Technology Facilities Council, Rutherford Appleton Laboratory, Didcot OX11 0QX, United Kingdom; [i]The UK X-ray Materials Science Facility at the European Synchrotron Radiation Facility, Grenoble F-38043, France; [j]Department of Physics, University of Warwick, Coventry CV4 7AL, United Kingdom; [k]Department of Chemistry, University of Tennessee, Knoxville, TN 37916; [l]Courant Institute of Mathematical Sciences, New York University, New York, NY 10012; [m]Department of Physics, New York University, New York, NY 10003; and [n]Department of Chemistry, Case Western Reserve University, Cleveland, OH 44106

Author contributions: B.G. designed research; M.M., M.S.C., G.d.A.L.e.S., T.S., V.K., P.Q., A.P., S.P., and R.C.K. performed research; M.M., M.S.C., G.d.A.L.e.S., T.S., V.K., P.Q., J.W., R.S., T.A.Z., M.D., S.G.G., J.R.-L., M.T., and B.G. analyzed data; and M.M., M.S.C., G.d.A.L.e.S., T.S., V.K., P.Q., R.S., T.A.Z., M.D., S.G.G., J.R.-L., M.T., and B.G. wrote the paper.

1. B. B. Hansen *et al.*, Deep eutectic solvents: A review of fundamentals and applications. *Chem. Rev.* **121**, 1232–1285 (2021), 10.1021/acs.chemrev.0c00385.
2. R. Ghahremani, R. F. Savinell, B. Gurkan, Perspective–Hydrogen bonded concentrated electrolytes for redox flow batteries: Limitations and prospects. *J. Electrochem. Soc.* **169**, 030520 (2022), 10.1149/1945-7111/ac58c6.
3. S. Kaur, A. Gupta, H. K. Kashyap, Nanoscale spatial heterogeneity in deep eutectic solvents. *J. Phys. Chem. B* **120**, 6712–6720 (2016), 10.1021/acs.jpcb.6b04187.
4. S. Spittle *et al.*, Evolution of microscopic heterogeneity and dynamics in choline chloride-based deep eutectic solvents. *Nat. Commun.* **13**, 219 (2022), 10.1038/s41467-021-27842-z.
5. Z. Hou *et al.*, Towards a high efficiency and low-cost aqueous redox flow battery: A short review. *J. Power Sources* **601**, 234242 (2024), 10.1016/j.jpowsour.2024.234242.
6. M. Mansha *et al.*, Recent developments on electroactive organic electrolytes for non-aqueous redox flow batteries: Current status, challenges, and prospects. *Chem. Record* **24**, e202300233 (2024), 10.1002/tcr.202300233.
7. C. D'Agostino, R. C. Harris, A. P. Abbott, L. F. Gladden, M. D. Mantle, Molecular motion and ion diffusion in choline chloride based deep eutectic solvents studied by ^{1}H pulsed field gradient NMR spectroscopy. *Phys. Chem. Chem. Phys.* **13**, 21383 (2011), 10.1039/c1cp22554e.
8. T. Cosby, A. Holt, P. J. Griffin, Y. Wang, J. Sangoro, Proton transport in imidazoles: Unraveling the role of supramolecular structure. *J. Phys. Chem. Lett.* **6**, 3961–3965 (2015), 10.1021/acs.jpclett.5b01887.
9. Z. Long, A. O. Atsango, J. A. Napoli, T. E. Markland, M. E. Tuckerman, Elucidating the proton transport pathways in liquid imidazole with first-principles molecular dynamics. *J. Phys. Chem. Lett.* **11**, 6156–6163 (2020), 10.1021/acs.jpclett.0c01744.
10. T. Cosby, Z. Vicars, M. Heres, J. Sangoro, Associating imidazoles: Elucidating the correlation between the static dielectric permittivity and proton conductivity. *Phys. Rev. Lett.* **120**, 136001 (2018), 10.1103/physrevlett.120.136001.
11. D. Marx, Proton transfer 200 years after von Grotthuss: Insights from ab initio simulations. *ChemPhysChem* **7**, 1848–1870 (2006), 10.1002/cphc.200600128.
12. H. Doi *et al.*, A new proton conductive liquid with no ions: Pseudo-protic ionic liquids. *Chemistry* **19**, 11522–11526 (2013), 10.1002/chem.201302228.
13. H. Watanabe *et al.*, Possible proton conduction mechanism in pseudo-protic ionic liquids: A concept of specific proton conduction. *J. Phys. Chem. B* **123**, 6244–6252 (2019), 10.1021/acs.jpcb.9b03185.
14. J. Ingenmey, S. Gehrke, B. Kirchner, How to harvest Grotthuss diffusion in protic ionic liquid electrolyte systems. *ChemSusChem* **11**, 1900–1910 (2018), 10.1002/cssc.201800436.

15. L. Wylie, M. Kéri, A. Udvardy, O. Hollóczki, B. Kirchner, On the rich chemistry of pseudo-protic ionic liquid electrolytes. *ChemSusChem* **16**, e202300535 (2023), 10.1002/cssc.202300535.
16. A. Noda *et al.*, Brønsted acid—base ionic liquids as proton-conducting nonaqueous electrolytes. *J. Phys. Chem. B* **107**, 4024–4033 (2003), 10.1021/jp022347p.
17. K. M. Johansson, E. I. Izgorodina, M. Forsyth, D. R. Macfarlane, K. R. Seddon, Protic ionic liquids based on the dimeric and oligomeric anions: [(AcO)xHx−1]−. *Phys. Chem. Chem. Phys.* **10**, 2972 (2008), 10.1039/b801405a.
18. F. Zhu *et al.*, Proton donor/acceptor effects on electrochemical proton-coupled electron transfer reactions at solid–liquid interfaces. *Curr. Opin. Electrochem.* **42**, 101377 (2023), 10.1016/j.coelec.2023.101377.
19. N. B. Lewis, R. P. Bisbey, K. S. Westendorff, A. V. Soudackov, Y. Surendranath, A molecular-level mechanistic framework for interfacial proton-coupled electron transfer kinetics. *Nat. Chem.* **16**, 343–352 (2024), 10.1038/s41557-023-01400-0.
20. X. Zhang, S. Zhou, F. M. Leonik, L. Wang, D. G. Kuroda, Quantum mechanical effects in acid–base chemistry. *Chem. Sci.* **13**, 6998–7006 (2022), 10.1039/d2sc01784a.
21. A. O. Atsango, M. E. Tuckerman, T. E. Markland, Characterizing and contrasting structural proton transport mechanisms in azole hydrogen bond networks using *Ab Initio* molecular dynamics. *J. Phys. Chem. Lett.* **12**, 8749–8756 (2021), 10.1021/acs.jpclett.1c02266.
22. M. Yoshizawa, W. Xu, C. A. Angell, Ionic liquids by proton transfer: Vapor pressure, conductivity, and the relevance of ΔpK_a from aqueous solutions. *J. Am. Chem. Soc.* **125**, 15411–15419 (2003), 10.1021/ja035783d.
23. H. Watanabe, N. Arai, H. Jihae, Y. Kawana, Y. Umebayashi, Ionic conduction within non-stoichiometric N-methylimidazole-acetic acid pseudo-protic ionic liquid mixtures. *J. Mol. Liq.* **352**, 118705 (2022), 10.1016/j.molliq.2022.118705.
24. T. Bjorholm, J. P. Jacobsen, 13C and 2H relaxation time studies of formic acid and acetic acid in water solution. Isotope effects on correlation times. *J. Magn. Reson.* **1969**, 237–251 (1980), 10.1016/0022-2364(80)90133-x.
25. A. Mitra, P. J. Seaton, R. Ali Assarpour, T. Williamson, Unprecedented concentration dependent chemical shift variation in1H-NMR studies: A caveat in the investigations of molecular recognition and structure elucidation. *Tetrahedron* **54**, 15489–15498 (1998), 10.1016/s0040-4020(98)01015-1.
26. Y. Erdogdu *et al.*, FT-IR, FT-Raman, NMR spectra and DFT simulations of 4-(4-fluoro-phenyl)-1*H*-imidazole. *Opt. Spectrosc.* **114**, 525–536 (2013), 10.1134/s0030400x13040073.
27. X. Sun *et al.*, Theoretical and experimental studies on proton transfer in acetate-based protic ionic liquids. *J. Mol. Liq.* **221**, 254–261 (2016), 10.1016/j.molliq.2016.05.080.
28. E. M. Morais, I. Abdurrokhman, A. Martinelli, Solvent-free synthesis of protic ionic liquids. Synthesis, characterization and computational studies of triazolium based ionic liquids. *J. Mol. Liq.* **360**, 119358 (2022), 10.1016/j.molliq.2022.119358.
29. S. K. Das *et al.*, Electronic fingerprint of the protonated imidazole dimer probed by X-ray absorption spectroscopy. *J. Phys. Chem. Lett.* **15**, 1264–1272 (2024), 10.1021/acs.jpclett.3c03576.
30. A. M. Stingel, P. B. Petersen, Couplings across the vibrational spectrum caused by strong hydrogen bonds: A continuum 2D IR study of the 7-azaindole–acetic acid heterodimer. *J. Phys. Chem. B* **120**, 10768–10779 (2016), 10.1021/acs.jpcb.6b05049.
31. D. Marx, M. E. Tuckerman, J. Hutter, M. Parrinello, The nature of the hydrated excess proton in water. *Nature* **397**, 601–604 (1999), 10.1038/17579.
32. J. Katsumi, T. Nakayama, Y. Esaka, B. Uno, Mechanistic study on the electrochemical reduction of 9, 10-anthraquinone in the presence of hydrogen-bond and proton donating additives. *Anal. Sci.* **28**, 257–265 (2012), 10.2116/analsci.28.257.
33. S. Pang, X. Wang, P. Wang, Y. Ji, Biomimetic amino acid functionalized phenazine flow batteries with long lifetime at near-neutral pH. *Angew. Chem. Int. Ed. Engl.* **60**, 5289–5298 (2021), 10.1002/anie.202014610.
34. M. H. V. Huynh, T. J. Meyer, Proton-coupled electron transfer. *Chem. Rev.* **107**, 5004–5064 (2007), 10.1021/cr0500030.
35. C. Costentin, J. M. Savéant, Multielectron, multistep molecular catalysis of electrochemical reactions: Benchmarking of homogeneous catalysts. *ChemElectroChem* **1**, 1226–1236 (2014), 10.1002/celc.201300263.
36. D. M. Prado, X. Shen, R. Savinell, C. Burda, Hydrodynamic voltammetry of Fe2+/3+ in aqueous deep eutectic solvents towards redox flow batteries. *Electrochim. Acta* **467**, 143082 (2023), 10.1016/j.electacta.2023.143082.
37. S. Pang *et al.*, A phenazine-based high-capacity and high-stability electrochemical CO2 capture cell with coupled electricity storage. *Nat. Energy* **8**, 1126–1136 (2023), 10.1038/s41560-023-01347-z.
38. X. Shen, N. Sinclair, J. Wainright, R. F. Savinell, Methods–Analyzing electrochemical kinetic parameters in deep eutectic solvents using an extended Butler-Volmer equation. *J. Electrochem. Soc.* **168**, 056520 (2021), 10.1149/1945-7111/ac006a.
39. N. A. Shaheen, M. Ijjada, M. B. Vukmirovic, R. Akolkar, Mechanism of electrochemical oxidation of nitroxide radicals in ethaline deep eutectic solvent. *J. Electrochem. Soc.* **167**, 143505 (2020), 10.1149/1945-7111/abc439.
40. X. Wu *et al.*, Diffusion-free Grotthuss topochemistry for high-rate and long-life proton batteries. *Nat. Energy* **4**, 123–130 (2019), 10.1038/s41560-018-0309-7.
41. P. Li *et al.*, Hydrogen bond network connectivity in the electric double layer dominates the kinetic pH effect in hydrogen electrocatalysis on Pt. *Nat. Catal.* **5**, 900–911 (2022), 10.1038/s41929-022-00846-8.
42. R. Dikki *et al.*, Composition–property relationships of choline based eutectic solvents: Impact of the hydrogen bond donor and CO_2 saturation. *Green Chem.* **26**, 3441–3452 (2024), 10.1039/d3gc04905a.
43. C. D. Dewhurst *et al.*, The small-angle neutron scattering instrument D33 at the Institut Laue-Langevin. *J. Appl. Crystallogr.* **49**, 1–14 (2016), 10.1107/s1600576715021792.
44. C. D. Dewhurst, Graphical reduction and analysis small-angle neutron scattering program: *GRASP*. *J. Appl. Crystallogr.* **56**, 1595–1609 (2023), 10.1107/s1600576723007379.
45. P. Qian *et al.*, Scanning electrochemical microscopy for kinetic investigations in viscous deep eutectic solvents: Identifying practical approach curves and deviations from electron transfer models. *Anal. Chem.* **97**, 16239–16249 (2025), 10.1021/acs.analchem.5c01310.
46. Y. Litman *et al.*, I-PI 3.0: A flexible and efficient framework for advanced atomistic simulations. *J. Chem. Phys.* **161**, 062504 (2024), 10.1063/5.0215869.
47. M. Munoz *et al.*, Structure, transport and electrochemical data of structured electrolytes based on imidazole and acetic acid mixtures. OSF. https://doi.org/10.17605/OSF.IO/5NRQH. Deposited 9 December 2025.